https://ntrs.nasa.gov/search.jsp?R=19700032024 2018-07-23T14:14:30+00:00Z

N 70 41340
CR 113922

CASE FILE
COPY

Precise Location of Sagittarius X-Ray Sources with a Rocket-borne Rotating Modulation Collimator

CSR-P-70-40

CENTER FOR SPACE RESEARCH
MASSACHUSETTS INSTITUTE OF TECHNOLOGY

Precise Location of Sagittarius X-Ray Sources with a Rocket-borne Rotating Modulation Collimator

CSR-P-70-40

Precise Location of Sagittarius X-Ray Sources with a Rocket-borne Rotating Modulation Collimator*

H. W. Schnopper, H. V. Bradt, S. Rappaport, E. Boughan,
B. Burnett, R. Doxsey, W. Mayer, and S. Watt

Department of Physics and Center for Space Research
Massachusetts Institute of Technology
Cambridge, Massachusetts 02139

Received 1970

ABSTRACT

We have measured with high precision (about 1' to 2') the celestial positions of four x-ray sources (GX3+1, GX5-1, GX9+1, GX17+2) in the Sagittarius region. The experiment was performed with two independent rocket-borne rotating modulation collimators backed with proportional counter detectors sensitive in the 1.5 to 8 keV energy range. High precision aspect data were obtained by star photography which was directly referenced to the collimator grids.

*This work was supported in part by the National Aeronautics and Space Administration under contract NSR 22-009-129 and Grant NGL 22-009-015.

The galactic center region is rich in x-ray sources. Mayer et al. (1970) give the most recent location results which, when taken together with those of other investigators (Gursky et al. 1967; Bradt et al. 1968a), yield positional error circles of between 10' and 20' radius (Table 1). These investigators have used narrow field of view slat collimator telescopes, but in our experiment the central feature is the wide field and high resolution of a spinning (Mertz 1967; Schnopper et al. 1968) modulation collimator (Oda, 1965; Bradt et al. 1968b) with precise aspect data provided by photography which simultaneously images the star field and the collimator grid system (Gursky et al. 1966). The principal objective of our experiment was the precise determination of the celestial positions of two of the brighter Sagittarius sources, GX5-1 and GX9+1.

The payload consists of two independent modulation collimator/aspect systems (Fig. 1) and a single slat collimator system. The coarser (wire-wound) collimator has planes of maximum transmission separated by $8\overset{'}{.}078 \pm .010$ and the finer (electroformed) has planes separated by $4\overset{'}{.}141 \pm .002$. For each system, the overall field of view is restricted to approximately 13° x 17° FWHM by additional slats. The slat collimator experiment is used for coarse source location and is similar in construction to the one described by Mayer et al. (1970).

Behind each collimator are two proportional counter detectors each having a 50μ Be window and a detecting gas

consisting of a mixture of 75% A, 15% Xe, and 10% CH_4 at one atmosphere pressure. In the "head on" position, the unobstructed detection area is about 100 cm^2 for the 4' system and about 150 cm^2 for the 8' system. Each detector consists of electrically independent front and rear compartments. Data are taken from the front compartment (about 2 cm deep) of each detector and the front and rear compartments of each detector are connected in anticoincidence in order to reduce contributions from spurious events. Pulse height discriminators limit the energy range of photons accepted to 1.5 - 8 keV.

The central portion of each grid is removed to permit star photography (Fig. 1). In addition, two small regions of the grid on either side of the aperture are illuminated by diffuse light which is diffracted and shadowed by both grids and then imaged on the film as a set of fiducial bands which bracket the star field (Gursky et al. 1966). A laboratory calibration has determined that the unexposed bands on the film correspond to transmission planes of the collimator. In particular, for the purposes of aspect analysis, one band is identified as the fiducial transmission plane. The camera drive system operates once every 0.6 sec and the exposure is made for a duration of 0.5 sec. With this exposure stars of visual magnitude between 4.0 and 5.8 give useable trailed images (1' to 2') at rotation rates on the order of 1° per sec. Since it is possible to establish temporally as well as spatially the center of the trail the collimator aspect

derived from each frame can be determined within an error of about 20". These aspect data can then be smoothed by Fourier techniques. A linear interpolation is used for times which occur between aspect determinations.

On 2 October 1969 at 8:24 P.M., MDT, the experiment was launched aboard an Aerobee 150 rocket fired from the White Sands Missile Range. A small portion (about 10 sec) of the observing time was devoted to a rapid scan (6° per sec) over the region containing Sco X-1. With aspect data which were degraded by the rapid rotation rate and the absence of a sufficient number of bright stars in the field of view, it is still possible to place individual lines of position on the celestial sphere with an accuracy of 50". The most probable position indicated by our data is 2'.5 from Sco X-1. The largest component of this error is along the lines of position and it is due to the incomplete (60°) rotation. The remainder of the time (about 190 sec at 1°.2 per sec) was used to view the Sagittarius region near the galactic center. A histogram of a portion of the data obtained from the 8' collimator is shown in Figure 2.

A correlation technique, discussed by Mertz (1967) is modified to meet the conditions of a drifting axis of rotation and a multiple source field. The analysis is based on the cross-correlation of the observed data with a trial function which is generated under the assumption that a source is located at a chosen point on the celestial sphere.

The expectation value of the counting rate N(t) at time t shown in Figure 2 is of the form:

$$\langle N(t)\rangle = \sum_i a_i f_i(t) + b \tag{1}$$

where a_i is the observed peak counting rate which is due to the ith source, $f_i(t)$ is the exposure function for the ith source at time t, and b is the background counting rate.

To define $f_i(t)$, let $\vec{c}$ be the vector representing the fiducial view direction at time t, $\vec{n}$ be a vector perpendicular to both $\vec{c}$ and the grid wires in the collimator, and $\vec{s}_i$ be a vector in the direction of the ith source (or trial) position. Also let Δ be the collimator period in radians, and g_i be the number of periods between $\vec{s}_i$ and the fiducial transmission plane at time t. With these definitions, $g_i = (1/\Delta)|\vec{n}\cdot\vec{s}_i/\vec{c}\cdot\vec{s}_i|$, and $f_i = |1-2(g_i-[g_i])|$, where $[g_i]$ = largest integer $\leq g_i$. The trial function f_p is just the exposure function for the trial position p on the celestial sphere.

We follow Lee (1960) and define the cross-correlation function $C_p(\tau)$ for the trial position p as

$$C_p(\tau) = \int_{T_1}^{T_2} N(t+\tau) f_p(t)\,dt. \tag{2}$$

Further, the integrated exposure E_p is defined as

$$E_p = \int_{T_1}^{T_2} f_p(t)\,dt. \tag{3}$$

Since phase information is contained in the choice of p, only cases for which $\tau=0$ need be considered.

Sources are found by constructing maps of a new function $U_p = C_p(0)/E_p$ for an array of points in a candidate region. Each source is characterized by a ring pattern which is centered on the source position and which has a radial periodicity given approximately by Δ. Once the bright sources have been located, their ring patterns can be removed from the map. "Subtracted" maps are computed from the function V_p defined as

$$V_p = \frac{C_p(0) - \sum_i a_i \int_{T_1}^{T_2} f_p(t) f_i(t)\,dt}{E_p} \tag{4}$$

The map shown in Figure 3a is computed from U_p. The source GX5-1 is clearly visible. The maps shown in Figures 3b, 4 and 5 are computed from Equation 4 according to the conditions listed in the captions. The source positions are measured from maps similar to those shown in Figure 5.

The behavior of the maps can be studied analytically if an ideal experiment is assumed. In this case the spin axis remains fixed and the rate of rotation ω is constant, and Equation 1 becomes

$$\langle N(t)\rangle = \sum_i a_i \left\{ 1/2 + (4/\pi^2) \sum_{\text{odd } n} (1/n^2) \cos[(2n\pi r_i/\Delta)\cos(\omega t - \theta_i)] \right\} \tag{5}$$

where r_i is the radial distance from the spin axis to the ith source measured in units of Δ and θ_i is the angular position at t=0. The term in braces is just the ideal $f_i(t)$. If the collimator is not completely opaque in the minimum transmission directions, then the higher frequency terms in the Fourier

spectrum given by Equation 5 do not contribute to the modulation. Thus a leaky collimator enhances the constant part of f_i and depletes the time varying part.

Since the ring patterns from all sources interfere, the source positions derived from a correlation analysis are not independent, e.g., the position of GX3+1 shifts by 0.'8 and the distribution sharpens considerably when the ring patterns for GX5-1 and GX9+1 are subtracted (Figs. 3a,b; 5, c and d). It is, therefore, important that the measured counting rate be accounted for either in terms of identified sources or a collimator leak, since an unidentified counting rate will cause small but unpredictable source position shifts. The leak contribution is determined to be about 10 percent from the pass over Sco X-1, and in this experiment approximately 3/4 of the counting rate has been identified. Other than the four x-ray sources listed in Table 1, no other major source is indicated in either of Figures 3a or b. We conclude, therefore, that the errors which are introduced by unidentified counting rate are small compared with 0.'8.

For the data from each collimator an error circle associated with the position of each source is derived from the statistical errors associated with the measurements of aspect and counting rate. The error circles listed in Table 1 are defined operationally by the contour which is three standard deviations down from the peak on maps similar to those shown in Figure 5. The standard deviation is determined empirically from a region of the map which does not contain a source. The

radial error listed in Table 1 is due to the uncertainties in the measurement of Δ, therefore, the error circle should be elongated along the radial line towards the approximate center of rotation ($\ell^{II}=6\overset{\circ}{.}7$; $b^{II}=-2\overset{\circ}{.}0$). Finally, in Table 1 we present a weighted average position with an error circle which also allows for the possibility of systematic errors of as much as 20".

Two sources (GX9+9 and GX13+1) listed by other investigators did not contribute at least an identifiable correlation pattern in the error boxes assigned by Mayer et al. (1970). This result is consistent with expectations since GX9+9 was almost at the edge of the field of view of the coarse collimator, and the GX13+1 intensity would yield a correlation peak near the detection threshold.

We thank Mr. D. Humphries and Mr. G. Polucci for their creative contributions to the mechanical design of the payload; Mr. J. Carroll for his analysis of the peak position data; Mr. R. Thompson for his many discussions concerning data analysis; the staffs of Goddard Space Flight Center and the White Sands Missile Range for their operational support.

Table 1

Positions and Intensities of Observed X-Ray Sources

Source	Collimator	Coordinates α 1950	Coordinates δ 1950	Coordinates ℓ^{II}	Coordinates b^{II}	Radial Error	Error Circle Radius Present	Error Circle Radius Previous[a]	Source Strength[b]	N_σ[c]
GX3+1	4'	$17^h44^m50^s$	-26°32.'9	2.°294	0.°790	0.'15	1.'0	20'	0.39	8
	8'	17 44 46	-26 33.3	2.282	0.797	0.40	1.9		0.29	6
Weighted Average		17 44 49	-26 33.0	2.291	0.792	--	1.7		--	-
GX5-1	4'	17 58 04	-25 04.5	5.083	-1.021	0.06	0.5	10	1.00	27
	8'	17 58 02	-25 05.0	5.070	-1.016	0.14	0.9		1.00	29
Weighted Average		17 58 04	-25 04.7	5.079	-1.020	--	1.2		--	--
GX9+1	4'	17 58 36	-20 31.7	9.081	1.147	0.12	1.0	20	0.32	7
	8'	17 58 33	-20 31.0	9.085	1.163	0.30	1.8		0.35	8
Weighted Average		17 58 35	-20 31.5	9.082	1.152	--	1.7		--	-
GX17+2	4'	18 13 10	-14 03.1	16.433	1.282	0.30	1.8	15	0.44	4
	8'	18 13 11	-14 02.7	16.440	1.283	0.76	2.0		0.79	7
Weighted Average		18 13 10	-14 03.0	16.435	1.282	--	2.6		--	-

[a]Mayer *et al.* (1970). 90 percent confidence level.

[b]Relative to GX5-1.

[c]Number of standard deviations above the average counting rate.

Figure Captions

Figure 1. One of the two independent modulation collimator systems on the payload. The galactic center region was viewed while the payload rotated about the pitch axis.

Figure 2. A histogram of a portion of N(t) obtained from the 8' collimator compared with the predicted curves obtained from the positions given in Table 1.

Figure 3. Maps derived from the 8' collimator data for the region $-4° \leq \ell^{II} \leq 18°$ and $-3° \leq b^{II} \leq 3°$ which contains all the sources identified in Table 1. The solid lines define $\ell^{II}=0$ and $b^{II}=0$. (a) U_p, (b) V_p derived from U_p by subtracting the contributions from GX5-1 and GX9+1. Only the sources listed in Table 1 had identifiable correlation patterns in both the 4' and 8' data. High values of U_p or V_p are indicated by light areas.

Figure 4. Detailed maps of $1\overset{\circ}{.}5 \times 1\overset{\circ}{.}5$ regions centered on the positions reported by Mayer <u>et al</u>. (1970). (a) GX5-1; U_p, (b) GX9+1; V_p with GX5-1 subtracted, (c) GX3+1; V_p with GX5-1 and GX9+1 subtracted, (d) GX17+2; V_p with GX5-1 and GX9+1 subtracted. The 4' data were calculated every $1\overset{'}{.}5$ and interpolated by Fourier analysis to $0\overset{'}{.}75$. The 8' data were calculated every $2\overset{'}{.}0$ and interpolated to $1\overset{'}{.}0$ for GX3+1 and GX17+2 and

calculated every $3'.0$ and interpolated to $0'.75$ for GX5-1 and GX9+1. In each map the average value is suppressed and the grey scale is divided into eighteen increments.

Figure 5. (a) A contour map of U_p for GX5-1. The contours are plotted in units of 3 counts per sec starting at a minimum (minus signs) of 415 counts per sec. Every fifth contour is dashed. (b) Lines of position for GX5-1 which are derived only from the peaks of N(t) and the aspect data. The central intersection lies at the same position of GX5-1 given in Table 1. (c) A contour map of the function U_p for GX3+1. (d) A contour map of V_p which is derived from U_p by subtracting the contributions from GX5-1 and GX9+1. The contours are plotted in units of 1 count per sec starting at a minimum of 430 in (c) and 293 in (d). Every fifth contour is dashed. The source positions given in Table 1 were taken from similar maps of V_p. The data shown here are all from the 8' collimator.

References

1. Bradt, H., Naranan, S., Rappaport, S. and Spada, G., 1968a, Ap. J., 152, 1005.

2. Bradt, H., Garmire, G., Oda, M., Sreekantan, B.V., Gorenstein, P. and Gursky, H., 1968b, Space Sci. Rev. 8, 471.

3. Gursky, H., Giacconi, R., Gorenstein, P., Waters, J.R., Oda, M., Bradt, H., Garmire, G., and Sreekantan, B.V., 1966, Ap. J., 144, 1249.

4. Gursky, H., Gorenstein, P., and Giacconi, R., 1967, Ap. J. (Letters), 150, L75.

5. Lee, Y.W., 1960, Statistical Theory of Communication, (New York: John Wiley and Sons), p.43.

6. Mayer, W., Bradt, H.V. and Rappaport, S., 1970, Ap. J. (Letters), 159, L115.

7. Mertz, L., 1967, Modern Optics (New York: Brooklyn Polytechnic Press), p.787.

8. Schnopper, H.W., Thompson, R.I., and Watt., S., 1968, Space Sci. Rev. 8, 534.

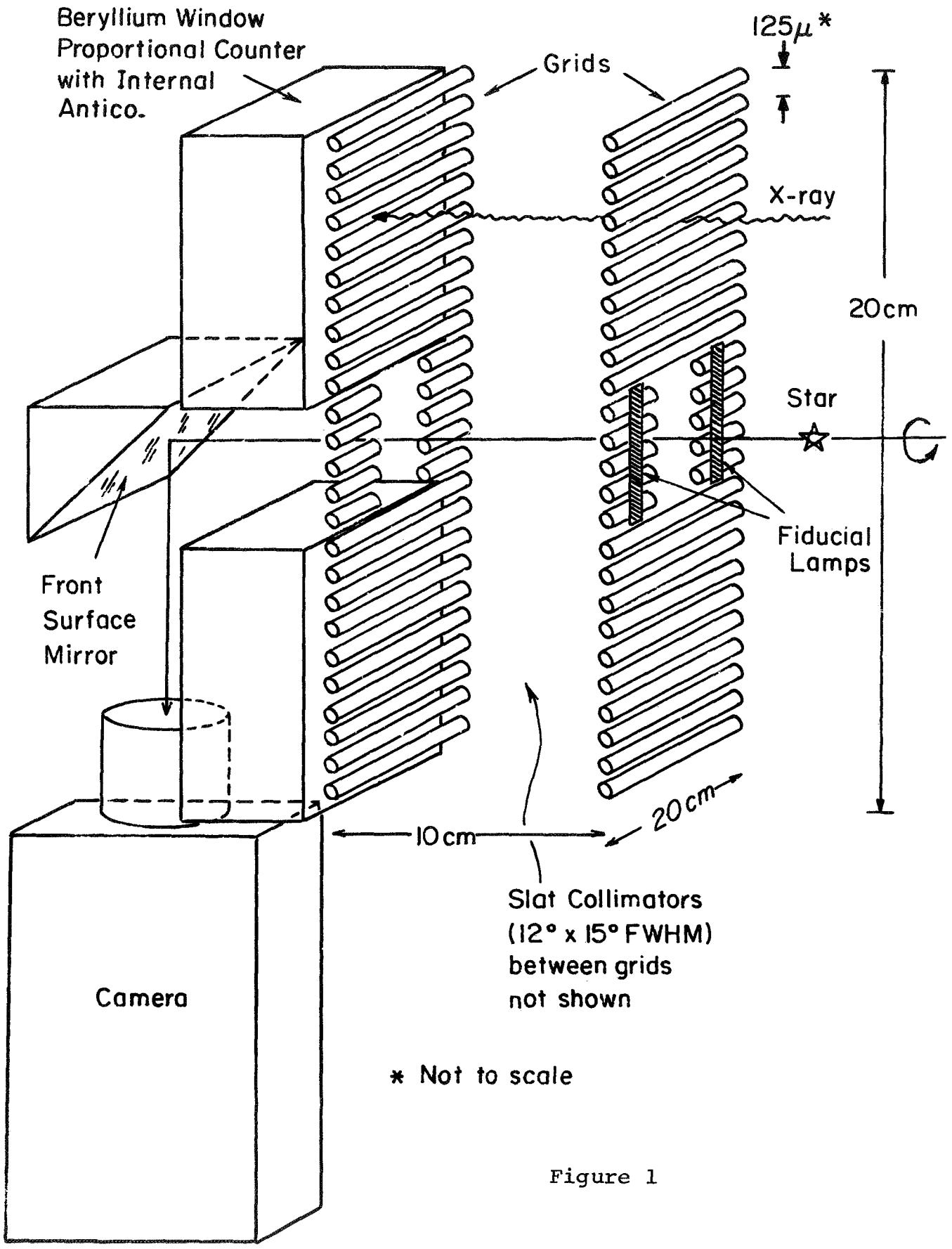
Beryllium Window
Proportional Counter
with Internal
Antico.
Grids
125μ*
X-ray
20cm
Star
Fiducial
Lamps
Front
Surface
Mirror
10cm
20cm
Slat Collimators
(12° x 15° FWHM)
between grids
not shown
Camera
* Not to scale

Figure 1

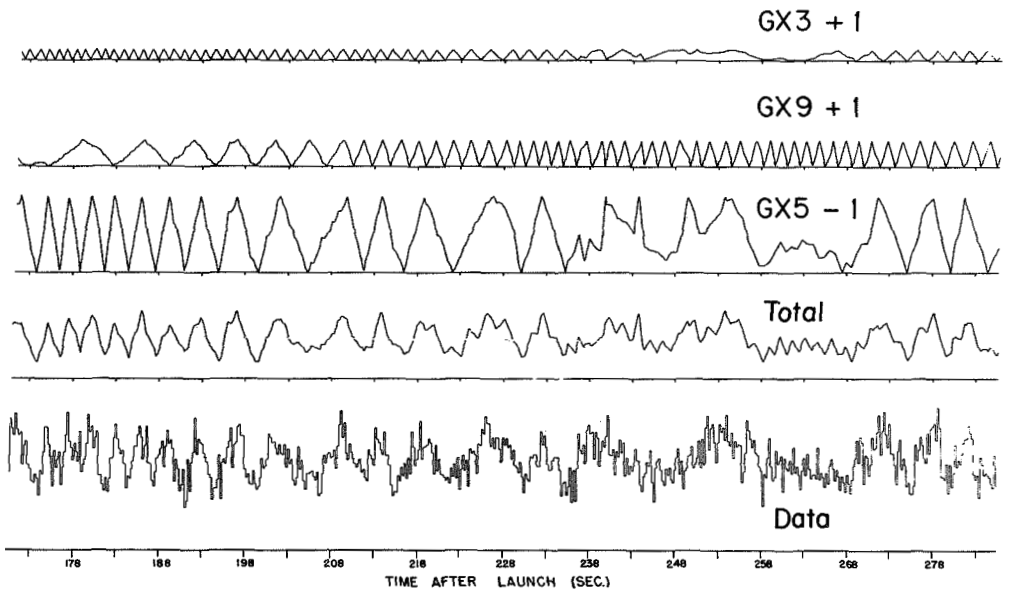
GX3 + 1
GX9 + 1
GX5 − 1
Total
Data
178
188
198
208
218
228
238
248
258
268
278
TIME AFTER LAUNCH (SEC.)

Figure 2

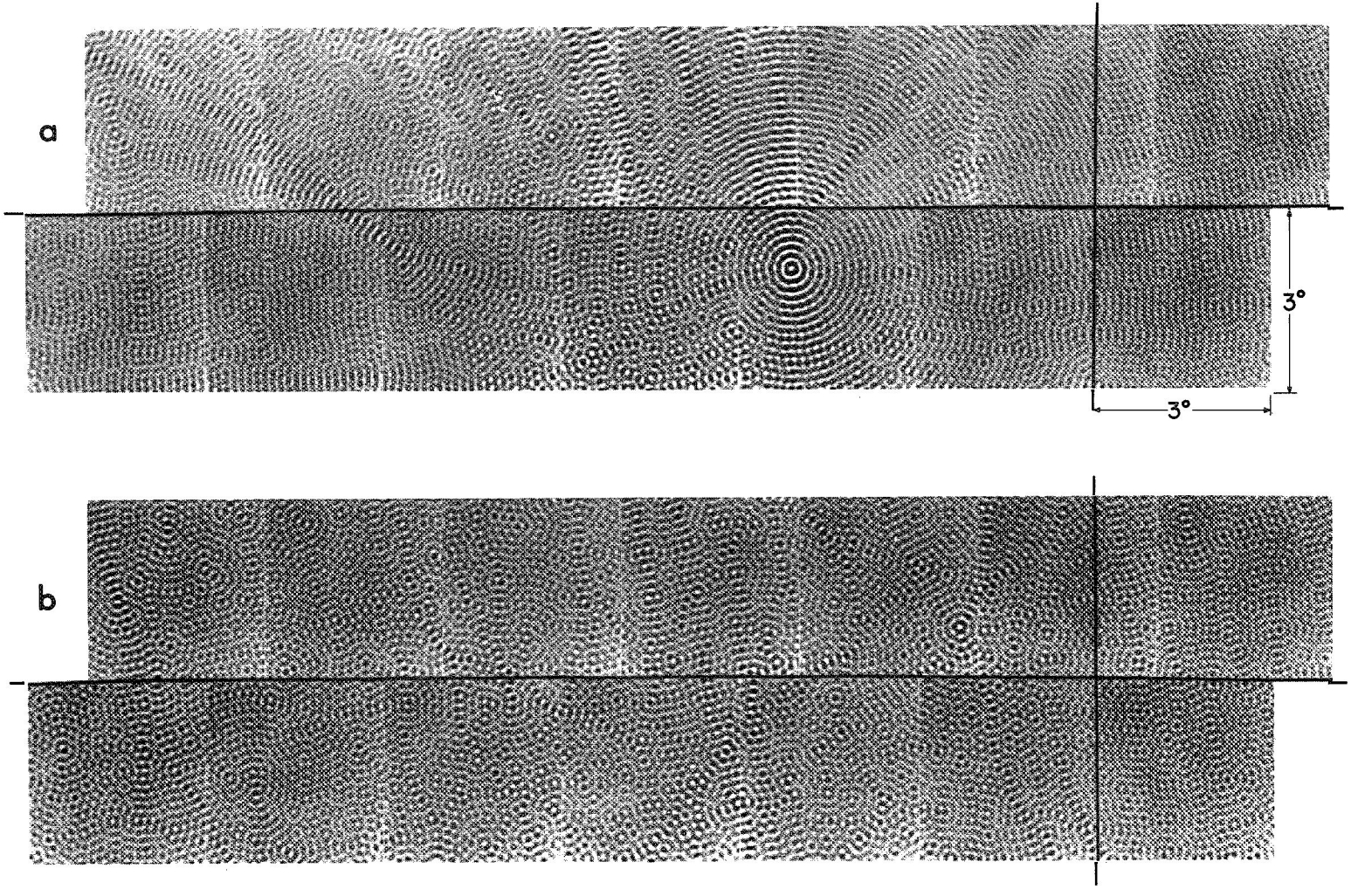

Figure 3

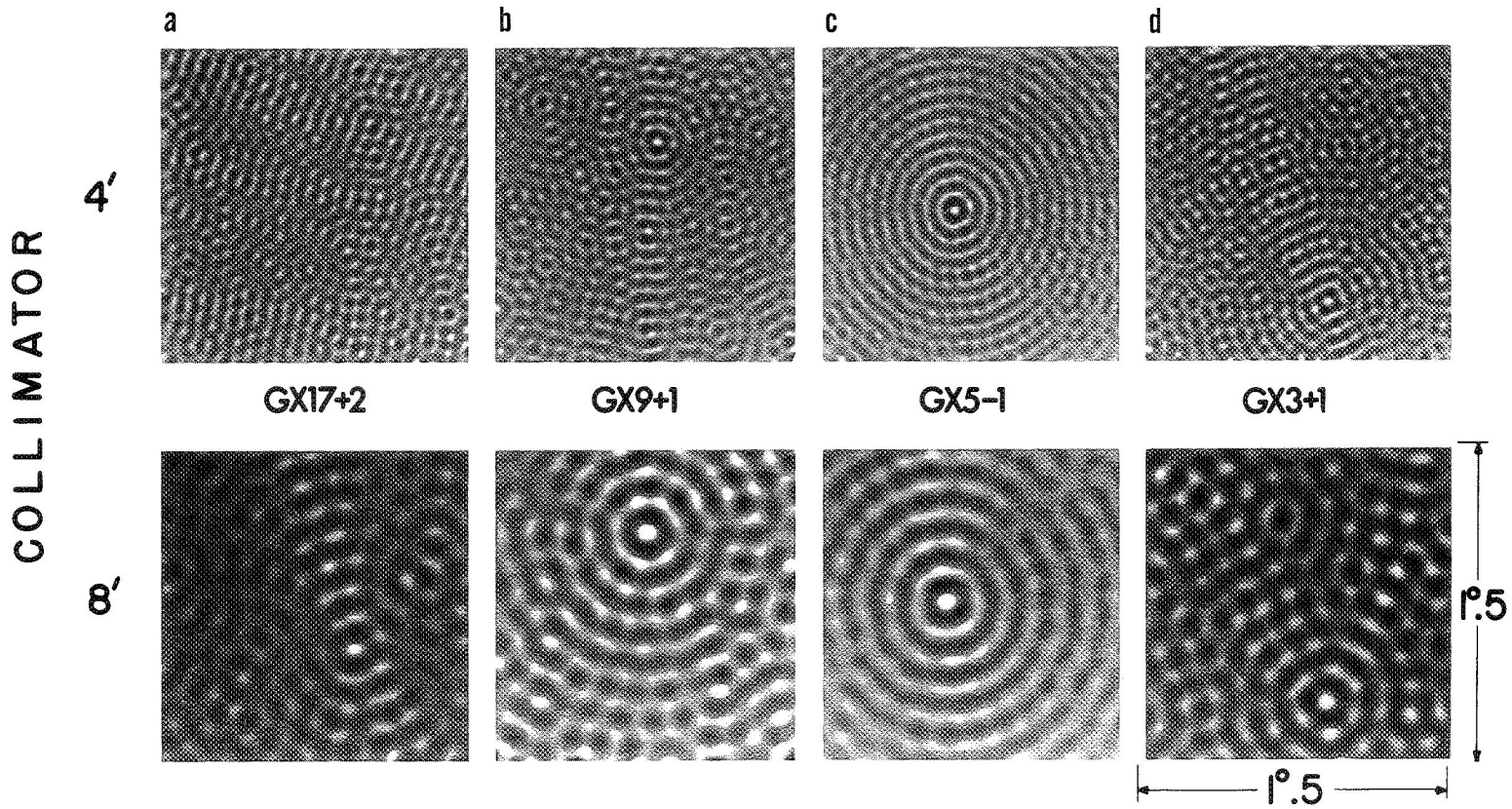

Figure 4

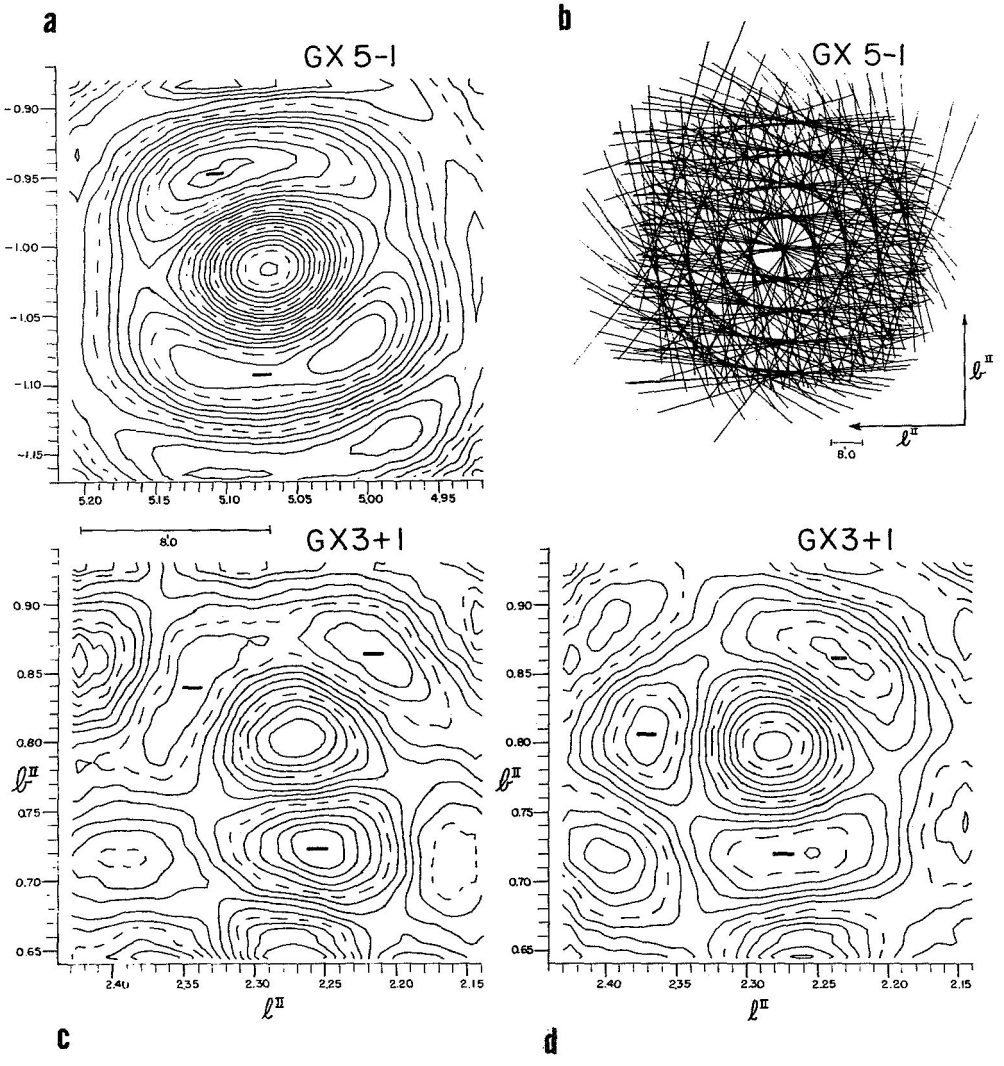

Figure 5